DISCLAIMER

This report was prepared as an account of work sponsored by an agency of the United States Government. Neither the United States Government nor any agency thereof, nor any of their employees, makes any warranty, express or implied, or assumes any legal liability or responsibility for the accuracy, completeness, or usefulness of any information, apparatus, product, or process disclosed, or represents that its use would not infringe privately owned rights. Reference herein to any specific commercial product, process, or service by trade name, trademark, manufacturer, or otherwise does not necessarily constitute or imply its endorsement, recommendation, or favoring by the United States Government or any agency thereof. The views and opinions of authors expressed herein do not necessarily state or reflect those of the United States Government or any agency thereof. Reference herein to any social initiative (including but not limited to Diversity, Equity, and Inclusion (DEI); Community Benefits Plans (CBP); Justice 40; etc.) is made by the Author independent of any current requirement by the United States Government and does not constitute or imply endorsement, recommendation, or support by the United States Government or any agency thereof.

SANDIA REPORT
SAND2025-11076
Printed September 2025

High-Fidelity Simulations of a Mach 9 Shock-Turbulent Boundary Layer Interaction

Cory Stack, Ross Wagnild

Prepared by
Sandia National Laboratories
Albuquerque, New Mexico 87185
Livermore, California 94550

Issued by Sandia National Laboratories, operated for the United States Department of Energy by National Technology & Engineering Solutions of Sandia, LLC.

Available to DOE and DOE contractors from

U.S. Department of Energy
Office of Scientific and Technical Information
P.O. Box 62
Oak Ridge, TN 37831

Telephone:	(865) 576-8401
Facsimile:	(865) 576-5728
E-Mail:	reports@osti.gov
Online ordering:	http://www.osti.gov/scitech

Available to the public from

U.S. Department of Commerce
National Technical Information Service
5301 Shawnee Road
Alexandria, VA 22312

Telephone:	(800) 553-6847
Facsimile:	(703) 605-6900
E-Mail:	orders@ntis.gov
Online order:	https://classic.ntis.gov/help/order-methods

ABSTRACT

High-fidelity large-eddy simulations (LES) and wall-modeled large-eddy simulations (WMLES) are performed on the interaction of a Mach 9 turbulent boundary layer with a 34^o compression ramp. Our primary interest is the sensitivity of mean and unsteady wall quantities to grid density. Additionally within the context of WMLES, we seek to explore solution sensitivity to the wall-model exchange location. It is shown that the mean LES wall quantities are sensitive to grid density, particularly in regions of large flow gradients. In contrast, mean WMLES wall quantities are shown to exhibit less variation due to grid density, and instead demonstrate significant sensitivity to the choice of wall-model exchange location. Comparisons between LES and WMLES results demonstrate that the separation length and peak heating are overpredicted by WMLES. We find that WMLES can reasonably reproduce the wall pressure fluctuation dynamics observed in LES for all considered grid densities.

Acknowledgment

The authors are grateful for the funding provided through the Advanced Simulation and Computing Verification and Validation portfolio, and are thankful for the computing allocation to the Lawerence Livermore National Laboratory Sierra platform through the Advanced Technology Computing Campaign.

LIST OF FIGURES

Variables

f Frequency

Φ Power spectral density

ρ Density

τ Shear stress

δ Boundary layer thickness

δ^* Displacement thickness

θ^* Momentum thickness

Subscripts

∞ Freestream quantity

e Boundary layer edge quantity

r Recovery

x Streamwise direction

y	Wall-normal direction
z	Lateral direction
w	Wall
0	Inflow quantity

1. INTRODUCTION

Shock-turbulent boundary layer interactions (STBLI) are ubiquitous in high speed flight. The aerodynamic impacts of these interactions on the vehicle body can be substantial, including increased structural loading and heating [8]. These impacts become more intense in separated STBLIs, where the low-frequency meandering of the shock foot at the separation location causes large local oscillations of the pressure field, while downstream flow reattachment causes a sharp rise in wall heat flux. At hypersonic conditions, these impacts can become further exacerbated due to the nonlinear dependence of flow conditions across the shock. These modulations to mechanical and thermal vehicle loading have resulted in catastrophic failures [5, 18], thus understanding the dynamics of these interactions is critical for vehicle resiliency.

Conventional engineering-grade analysis of STBLI are often performed using Reynolds-Averaged Navier Stokes (RANS) simulations. However, this approach is well known for its inaccurate prediction of flow separation [9, 10, 20, 15] and heat transfer [26, 12, 19]. This discrepancy results from the insufficient modeling of the myriad fluid dynamic phenomena throughout the interaction, including increased turbulence intensity across the shock, flow separation, shear layer development, separation bubble unsteadiness, and flow reattachment; wherein the modeling of these dynamics become less understood with increasing Mach number. Although there have been notable improvements to RANS models regarding heat flux predictions for hypersonic STBLIs [21, 25, 22], these models simply cannot predict unsteady aspects of the flow, particularly the modulation of wall pressure fluctuations through the interaction.

Scale-resolving high-fidelity simulations, such as direct numerical simulations (DNS) and large-eddy simulations (LES), have shown promise in their ability to accurately simulate the complex fluid dynamics within these interactions [23, 29, 24, 1, 2, 3, 11]. However, these modeling approaches are not practical for engineering applications due to the large computational cost associated with resolving the near-wall eddies, as well as attaining sufficient physical simulation time to converge low-frequency separation bubble statistics [11]. Another scale-resolving approach is wall-modeled large-eddy simulation (WMLES), wherein the computationally-costly near-wall eddies are modeled, while the outer-layer structures remain directly resolved at the grid scale. This leads to a dramatic reduction in grid resolution requirements compared to DNS and LES [7, 30], which subsequently lessens the time-step burden, thereby enabling scale-resolving simulations as substantially larger Reynolds numbers. However, there remains uncertainty with the ability of WMLES to predict engineering quantities of interest for these flows, such as wall shear stress, wall heat flux, and wall pressure fluctuations.

This study aims to assess these uncertainties by performing a suite of WMLES simulations of a Mach 9 turbulent boundary layer interacting with a 34^o compression ramp. A variety of grid densities are considered, as well as the sensitivity to wall model exchange location. Accompanying wall-resolved LES are also performed as a reference comparison to WMLES results. Additionally, a grid resolution study is performed for LES to assess solution sensitivity throughout the interaction.

2. METHODOLOGY

Our numerical model solves the three-dimensional, compressible, finite-volume representation of the Navier-Stokes equations using the Sandia Parallel Aerodynamics and Reentry code (SPARC) [14]. The low-dissipation 2^{nd}-order scheme of Subbareddy and Candler [28] is utilized to discretize the inviscid fluxes, while viscous fluxes are discretized with a 2^{nd}-order scheme, and time-integration is performed using a 2^{nd}-order implicit method. Shock capturing is facilitated by hybridizing the low-dissipation method with a 2^{nd}-order Steger-Warming flux [27] using the Larsson shock sensor [17]. An explicit subgrid scale model is not employed in this work. A synthetic turbulent boundary layer is imposed on the inflow plane using the synthetic digital filtering method (SDFM) of Adler *et al.* [4]. The statistics to initialize the SDFM are derived from a precursor RANS simulation. Wall-modeling is performed using an algebraic equilibrium wall function [6], and the wall-model exchange location is selected as either the wall-adjacent cell, or a location offset from the wall by 10% of the inflow boundary layer thickness (δ_0).

The flow conditions and geometry replicate those of Helm and Martin [13], wherein a Mach 9 turbulent boundary layer with the properties noted in Table 2-1 interacts with a 34^o compression ramp. Simulations are performed on several grids for LES and WMLES. For all cases, the inflow plane is located approximately $50\delta_0$ upstream of the corner, while the outflow plane is located $10\delta_0$ downstream of the corner.

Two grid densities are considered for the LES cases. For the first (LES-1), the grid spacing was based on the properties of the upstream boundary layer, with a target grid resolution of $\Delta x^+ = 15$, $\Delta z^+ = 10$, and $\Delta y_w^+ = 0.1$. The resulting grid spacings remain constant in the streamwise and spanwise directions throughout the domain, resulting in node counts in the streamwise, wall-normal, and spanwise directions of $(n_x, n_y, n_z) = (2041, 201, 255)$ for a domain spanning $5\delta_0$ in the spanwise direction. In effort to assess LES solution sensitivity to grid density, the second LES grid (LES-2) is refined within the interaction region, and the spanwise extent of the domain is increased to $10\delta_0$. Upstream of mean flow separation, the streamwise spacing remains consistent with LES-1, but downstream of separation, the streamwise grid spacing is reduced by a factor of four relative to LES-1. In the wall-normal direction, the number of points are increased from 201 to 301 in effort to better resolve large wall-normal gradients near reattachment. Lastly, the spanwise grid density of LES-2 was refined to coincide with $\Delta z^+ = 5$ for the incoming boundary layer, culminating in an overall grid size of $(n_x, n_y, n_z) = (3201\ , 301,\ 1501)$. The time-averaged spatial distributions of the grid densities for the LES cases, normalized by the local time-averaged viscous length scale, are shown in Fig. 2-1. Upstream of the interaction, target grid resolutions are achieved. However within the interaction, grid spacings relative to the local viscous length scale vary widely as a result of the complex separation and reattachment process.

Four different grid densities are considered for the WMLES cases (see Table 2-2). The baseline WMLES grid density was chosen based on the general recommendation of Larsson [16], wherein

M_e	$\rho_e[kg/m^3]$	$U_e[m/s]$	T_w/T_r	$\delta_0(mm)$	$\delta^*(mm)$	$\theta(mm)$	Re_τ
9	0.0403	1410.7	0.33	18.0	3.6	0.688	476

Table 2-1. Boundary layer properties and wall conditions for the LES and WMLES cases.

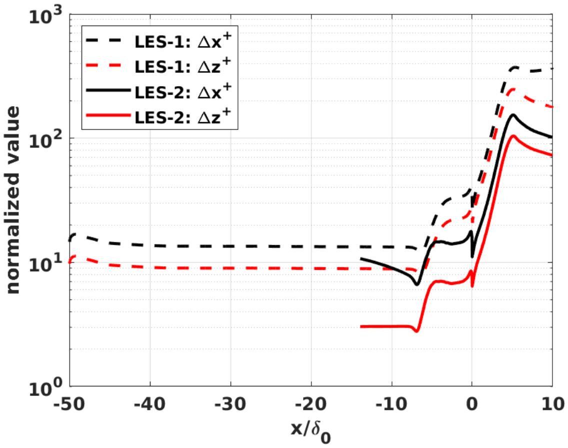

Figure 2-1. Streamwise and spanwise grid resolution of the LES cases throughout the simulation domain.

21 nodes per incoming boundary layer thickness are placed in the streamwise and spanwise directions ($n_x/\delta_0 = n_z/\delta_0 = 21$), and 51 equispaced nodes in the wall-normal direction within the boundary layer region ($n_{bl} = 51$). Relative to the baseline WMLES grid, the remaining three grids are refined in either the streamwise ('st'), wall-normal ('n'), or spanwise ('sp') direction, with grid density remaining constant in the other two directions. Grid densities are generally doubled with refinement, with the sole exception of the streamwise-refined case, which was cutoff at the streamwise resolution as the LES case. For all WMLES cases, the grid domain spans $5\delta_0$ in the spanwise direction. As documented in Stack *et al.* [6], for the region upstream of the interaction, wall-model exchange locations for the first-cell cases reside in the viscous sublayer ($y^+ < 5$), while exchange locations for offset cases are located at $y^+ \approx 300$.

WMLES Case	n_x/δ_0	n_{bl}	n_z/δ_0	n_x	n_y	n_z	Δx^+	Δz^+
Baseline	21	51	21	1201	101	101	20	20
Streamwise refined ('st')	35	51	21	2041	101	101	12	20
Wall-normal refined ('n')	21	101	21	1201	151	101	20	20
Spanwise refined ('sp')	21	51	41	1201	101	201	20	10

Table 2-2. Grid parameters for the WMLES grids. The subscripts x, y and z denote the streamwise, wall-normal and spanwise directions, while n_{bl} denotes the number of wall-normal nodes within the boundary layer. Grid spacings in viscous units are evaluated upstream of the interaction.

3. RESULTS

3.0.1. Flow Structure

An assessment of the overall flow structure can be seen in Fig. 3-1. The coordinate system shown in this figure denotes the convention for the remainder of the paper, with the streamwise direction as x, the spanwise direction as z, and the ramp begins at $x = 0$. The temperature contours in Fig. 3-1a highlight the incoming turbulent boundary layer and large-scale flow separation near the corner, and have an isocontour of the shock sensor to depict flow compression, including the ramp-generated shock and acoustic radiation from the boundary layer. The instantaneous wall pressure fluctuation normalized by the local mean pressure is shown in Fig. 3-1b. Upstream of the interaction, localized high-amplitude alternating positive-negative structures (APNS) previously documented in high-speed cold-wall hypersonic turbulent boundary layers [31] are observed (see dashed boxes). These structures generate the primary pressure fluctuations upstream of the interaction, and as shown below, exhibit a distinct signature in pressure fluctuation statistics. Downstream of the interaction, there is a rapid increase of pressure fluctuation amplitude, resulting in fluctuations occurring at a substantial fraction of the local mean pressure.

3.0.2. Mean Flow

Comparisons between the cases are first performed within the context of mean wall quantities (Fig. 3-2), where the top plots depict the full flowfield domain, and the bottom plots highlight the interaction region. Beginning with the comparison of LES-1 and LES-2 results, we see decent agreement in the separation point (Fig. 3-2a), but within the interaction, these simulations agree less well. This is particularly evident for $x/\delta_0 \geq 5$, which coincides with the impingement of the separation shock on the ramp (see Fig. 3-1a). In this region, grid density plays a substantial role in resolving the compression/expansion dynamics that dictate the peak wall shear stress, heat flux, and wall pressure, which set conditions for the subsequent downstream flow dynamics.

The assessment of the WMLES results can also be gleaned from Fig. 3-2, where results using the wall-adjacent cell (*i.e.* first-cell) as the wall-model exchange location are in blue, while results with the exchange location at $0.1\delta_0$ are in red (*i.e.* offset-based). Upstream of the interaction, we observe that offset-based cases result in better predictions of the the mean shear stress (Fig. 3-2a) and mean heat flux (Fig. 3-2b), while the effects of grid density are small, and only pronounced for first-cell WMLES cases, which are consistent with prior results [6]. However when the interaction begins, all WMLES cases prematurely predict separation (see Fig. 3-2a), while offset-based results generally give a better prediction than first-cell results. At the remaining locations downstream of the separation point, the choice of the exchange location appears to be a first-order effect when comparing mean wall quantities to LES, while grid refinement is

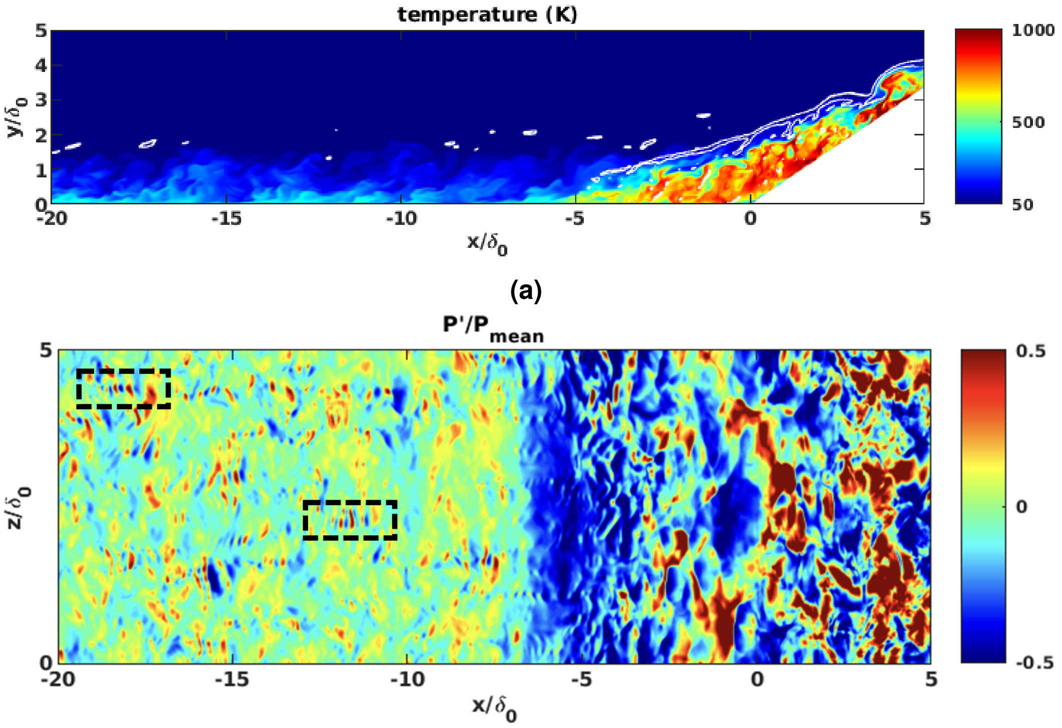

(a)

(b)

Figure 3-1. Realizations of the instantaneous LES flowfield: a) temperature contours with a white isocountour of the shock sensor, and b) wall pressure fluctuations normalized by the mean pressure, with black dashed boxes highlighting alternating positive-negative structures.

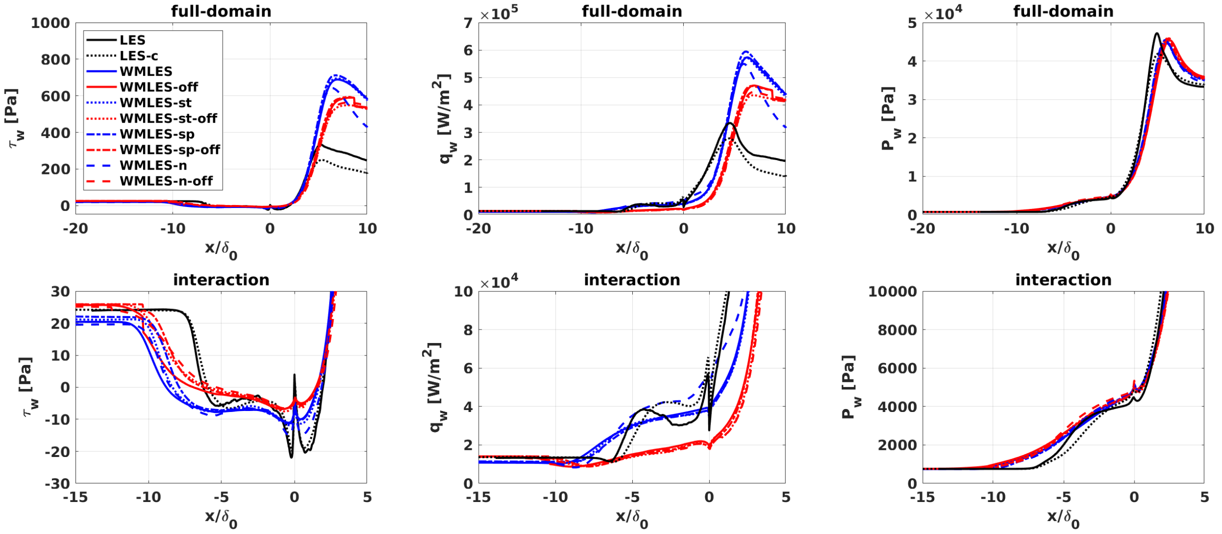

(a)

(b)

(c)

Figure 3-2. Mean wall quantities: a) shear stress, b) heat flux, and c) pressure. Top plots depict the full flowfield domain, and bottom plots highlight the interaction region.

secondary. These subtle differences between the cases associated with the interaction region are manifested in the mean wall pressure (Fig. 3-2c), where the larger separation region for the WMLES cases results in shock impingement further downstream on the ramp.

3.0.3. Unsteady Flow

The character of the unsteady flow field is first examined using the root-mean-square (RMS) of the wall pressure fluctuations (Fig. 3-3). Focusing on the LES results, we see the wall pressure fluctuation RMS first increases at separation, and continues to increase sharply until shock impingement on the ramp ($x/\delta_0 \sim 5$), after which it reduces. Smaller differences are observed in the LES wall pressure fluctuation RMS than the LES mean wall quantities, indicating the unsteady pressure field is less sensitive to grid density. Comparing WMLES to LES, upstream of the interaction, offset-based WMLES agrees well with LES, while first-cell WMLES underpredicts the wall pressure fluctuation RMS. Through the interaction, similar to the mean quantities, the premature flow separation for the WMLES cases leads to premature amplification of the wall pressure fluctuation RMS, and a similar streamwise peak shift as the mean wall pressure (Fig. 3-3b). The frequency dependence of these discrepancies will be further analyzed below.

Before comparing the WMLES wall pressure fluctuation power spectral density (PSD = $\Phi(f)$) to LES, we first analyze the LES wall pressure fluctuation PSD (Fig. 3-4). The normalized premultipled power spectral density (PPSD) of the wall pressure fluctuations are shown in Fig. 3-4a, where the spectrum at a given spatial location has been normalized to unit energy, and the frequency is nondimensionalized by the separation length and freestream velocity. Qualitatively, the wall pressure fluctuation PPSD follows that reported for spanwise-homogeneous STBLI [8, 1, 11], namely that upstream of the interaction ($x/\delta_0 < 10$) the spectrum comprises high-frequency integral-scale unsteadiness, while the separation location is dominated by low-frequency shock unsteadiness that is two orders-of-magnitude below that of the incoming turbulence, and the remainder of the interaction contains signatures of mid-frequency shear layer unsteadiness ($St_L \sim O(1)$). Additionally, our LES results agree well with the results of Helm and Martin [13], wherein separation point unsteadiness coincides with $St_L = 0.1$, and reattachment ($x/\delta_0 \sim 1$) is characterized by broadband mid-frequency unsteadiness.

The wall pressure fluctuation PSD provides a more quantitative assessment of the wall pressure fluctuations (Fig. 3-4b). For this figure, the upstream location was chosen as $x/\delta_0 = -14$, the separation and reattachment locations were selected based upon the mean wall shear stress, and the peak location coincides with the location of peak wall pressure fluctuation RMS. The wall pressure fluctuation PSD combines the results of the wall pressure fluctuation RMS and PPSD, wherein lower-amplitude broadband high-frequency fluctuations occur upstream of the interaction, and transition to larger-amplitude, low-frequency fluctuations at the separation point, followed by increasingly larger-amplitude broadband fluctuations until peak RMS is reached. Comparing the LES cases to each other, we observe good agreement for frequencies below $100kHz$, while above $100kHz$ we see worse agreement, particularly post-separation, which is not unexpected due to the reduced grid resolution of the LES-1 case.

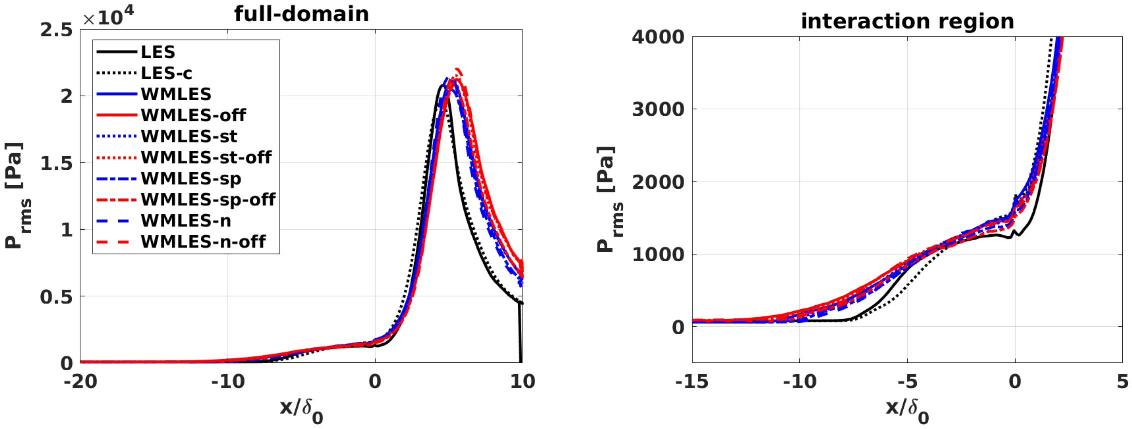

(a) (b)

Figure 3-3. Root-mean-square of wall pressure fluctuations.

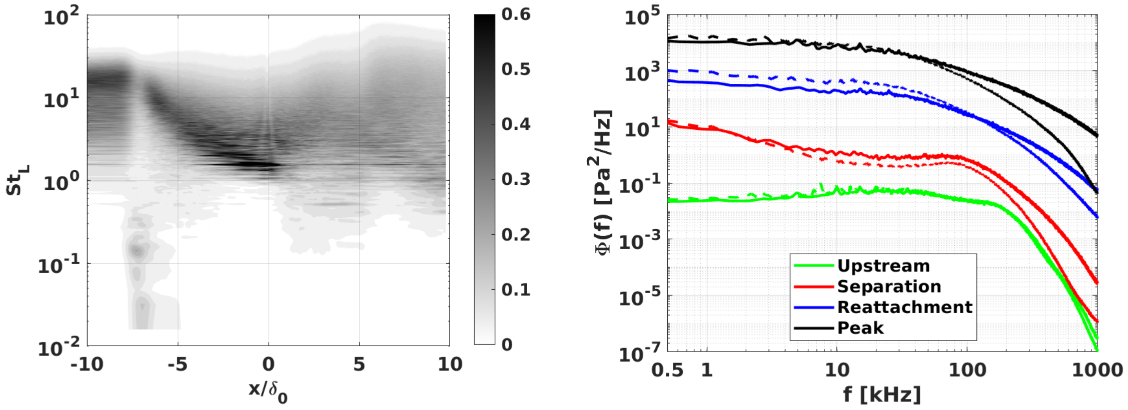

(a) (b)

Figure 3-4. LES wall pressure fluctuation spectra: a) normalized PPSD of the LES-2 case, b) PSD. The solid and dashed lines denote the LES-2 and LES-1 cases respectfully.

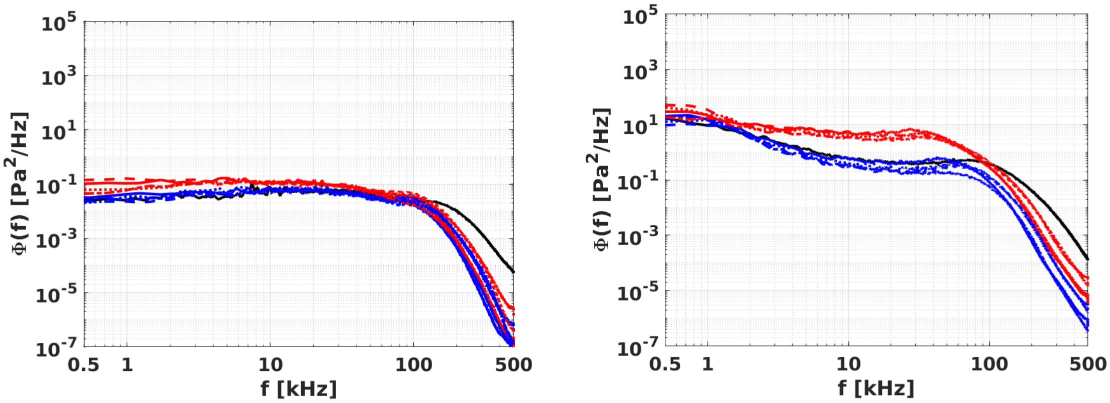

(a) Upstream **(b) Separation**

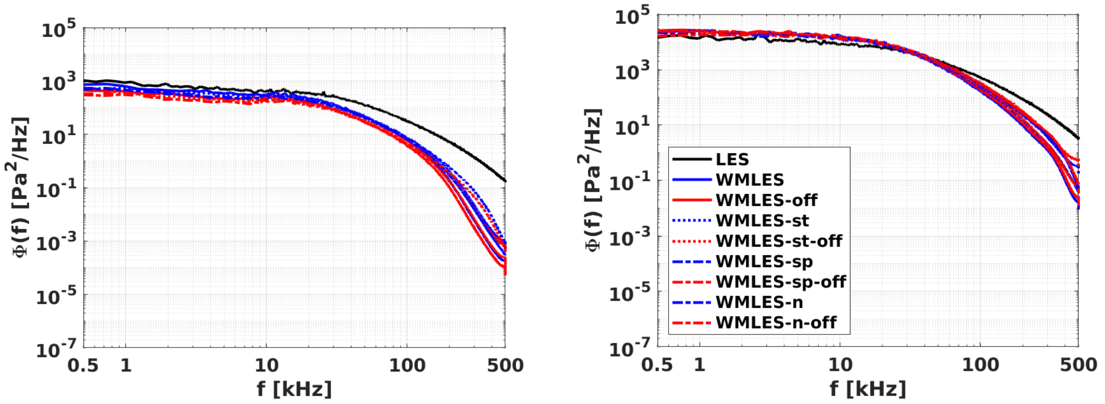

(c) Reattachment **(d) Peak P_{rms}**

Figure 3-5. Comparison of wall pressure fluctuation power spectral density between LES and WMLES at select spatial locations.

We now compare the wall pressure fluctuation PSD of the WMLES cases to the LES cases (Fig. 3-5). The same four locations of interest are utilized as before, and to maintain consistency between cases, the respective spatial locations corresponding to separation, reattachment, and peak wall pressure fluctuation RMS are derived from simulation data for each respective WMLES case. Upstream of the interaction (Fig. 3-5a), all WMLES cases underpredict the wall pressure fluctuation amplitude above $100kHz$, which is not unexpected due to the reduced near-wall resolution of the WMLES grids. However below this frequency, there is a noticeable difference between the WMLES cases, wherein the offset-based WMLES cases exhibit an upwards shift of the PSD curve relative to the LES and first-cell exchange WMLES cases (all of which agree well with LES). Given that all WMLES cases exhibit a similar rollover of the PSD curve at high frequencies, within the context of wall pressure fluctuation RMS, we can deduce that for offset-based cases, the increased fluctuation amplitude at low frequencies compensates for unresolved energy at higher frequencies, thus resulting in an improved agreement with LES wall pressure fluctuation RMS (Fig. 3-3). Thus, wall pressure fluctuation RMS alone is an inadequate metric to gauge the ability of WMLES to predict the unsteady wall pressure field, as the frequency dependence of these fluctuations plays a critical role in RMS contribution. At the separation point (Fig. 3-5b), a similar upwards shift of the offset-based WMLES cases is present, particularly near the $10kHz$ frequency range. At reattachment (Fig. 3-5c), all WMLES cases underpredict the fluctuation amplitude, although the first-cell exchange location WMLES generally exhibit a better comparison to LES. Lastly, comparing the PSD at peak wall pressure fluctuation RMS (Fig. 3-5d), all WMLES cases are in good agreement, although they slightly overpredict fluctuation amplitude below $10kHz$. Overall, these results demonstrate that WMLES can provide a reasonably comparable prediction of the low-frequency portion of the wall pressure dynamics beneath the STBLI relative to LES. However, solution sensitivity to wall modeling choices (*i.e.* selection of the exchange location, wall model type, etc.) needs to be further characterized at different conditions and configurations.

4. CONCLUSION

We performed high-fidelity large-eddy simulations (LES) and wall-modeled large-eddy simulations (WMLES) of a Mach 9 turbulent boundary layer interacting with a 34^o compression ramp. Grid sensitivity studies were performed for LES and WMLES cases. It was shown that grid density plays a substantial role in the prediction of mean LES wall quantities. In particular, the LES peak mean wall shear stress and peak mean wall heat flux differed by approximately 25% and 16% respectively, and slight differences in separation length resulted in different mean wall pressure distributions. However, the LES unsteady wall pressure dynamics were significantly less sensitive to grid density, as both databases reproduced previously reported Strouhal number regimes, including the imprint of the low-frequency shock foot oscillations ($St_L \sim O(0.1)$), mid-frequency separated shear layer structures ($St_L \sim O(1)$), and integral-scale boundary layer turbulence ($St_L \sim O(10)$) on the wall pressure field.

Our WMLES results demonstrate that the placement of the wall-model exchange location has a much larger impact on the flow predictions than the grid density. In particular, placing the exchange location away from the wall resulted in an improved comparison to mean LES wall quantities throughout the flow. However, placing the exchange location away from the wall resulted in a worse comparison to the power spectral density of LES wall pressure fluctuations throughout the flow. The results within this effort demonstrate that WMLES can reasonably reproduce the low and mid-frequency features of the interaction, however accurate prediction of the mean wall quantities using WMLES remains a challenge.

This page intentionally left blank.

REFERENCES

[1] M. C. Adler and D. V. Gaitonde. Dynamic linear response of a shock/turbulent-boundary-layer interaction using constrained perturbations. *Journal of Fluid Mechanics*, 840:291–341, 2018.

[2] M. C. Adler and D. V. Gaitonde. Dynamics of strong swept-shock/turbulent-boundary-layer interactions. *Journal of Fluid Mechanics*, 896, 2019.

[3] M. C. Adler and D. V. Gaitonde. Influence of separation structure on the dynamics of shock/turbulent-boundary-layer interactions. *Theor. Comput. Fluid Dyn.*, August 2021.

[4] M. C. Adler, D. R. Gonzalez, C. M. Stack, and D. V. Gaitonde. Synthetic generation of equilibrium boundary layer turbulence from modeled statistics. *Computers and Fluids*, 165:127–143, March 2018.

[5] J. J. Bertin and R. M. Cummings. Fifty years of hypersonics: where we've been, where we're going. *Progress in Aerospace Sciences*, 39:511–536, 2003.

[6] Stack C., M. Barone, R. Wagnild, and T. Fisher. Wall pressure fluctuation prediction for high-speed flows viawall-modeled large-eddy simulation. *AIAA SciTech Forum*, January 2025.

[7] H. Choi and P. Moin. Grid-point requirements for large eddy simulation: Chapman's estimates revisited. *Physics of Fluids*, 24, 011702, 2012.

[8] N. T. Clemens and V. Narayanaswamy. Low-frequency unsteadiness of shock wave/turbulent boundary layer interactions. *Annual Review of Fluid Mechanics*, 46:469–492, 2014.

[9] T. Coakley and P. Huang. Turbulence modeling for high speed flows. *30th Aerospace Sciences Meeting and Exhibit, AIAA Paper 1992-0436*, 1992.

[10] T. J. Coakley, C. C. Horstman, J. G. Marvin, J. R. Viegas, J.E. Bardina, P. G. Huang, and M. I. Kussoy. Turbulence compressibility corrections. *NASATM 108827*, 1993.

[11] D. V. Gaitonde and M. C. Adler. Dynamics of three-dimensional shock-wave/boundary-layer interactions. *Annual Review of Fluid Mechanics*, 55:291–321, 2022.

[12] P. A. Gnoffo, S. A. Berry, and J. W. Van Norman. Uncertainty assessments of hypersonic shock wave–turbulent boundary-layer interactions at compression corners. *AIAA Journal*, 50, 2013.

[13] C. M. Helm and M. P. Martin. Large eddy simulation of two separated hypersonic shock/turbulent boundary layer interactions. *Physical Review of Fluids*, 7:074601, 2022.

[14] M. Howard, T. Fisher, M. Hoemmen, D. Dinzl, J. Overfelt, A. Bradley, K. Kim, and S. Rajamanickam. Employing Multiple Levels of Parallelism for CFD at Large Scales on Next Generation High-Performance Computing Platforms. *ICCFD10*, 2018.

[15] C. J. Jordan, J. R. Edwards, and D. L. Stefanski. Evaluation of rans closure models with high-fidelity les datasets for hypersonic shock boundary layer interactions. *AIAA SciTech Forum , 2021-1666*, 2021.

[16] J. Larsson, S. Kawai, J. Bodart, and I. Bermejo-Moreno. Large eddy simulation with modeled wall-stress: recent progress and future directions. *Mechanical Engineering Reviews*, 3(1), 2016.

[17] J. Larsson, R. Vicquelin, and I. Bermejo-Moreno. Large Eddy Simulations of the HyShot II Scramjet. *Center For Turbulence Research, Annual Research Report Briefs*, 2011.

[18] I. A. Leyva. The relentless pursuit of hypersonic flight. *Physics Today*, 70:30–36, 2017.

[19] J. G. Marvin, J. L. Brown, and P. A. Gnoffo. Experimental databasewith baseline cfd solutions: 2-d and axisymmetric hypersonic shock-wave/turbulent-boundary-layer interactions. *NASA TM2013–216604*, 2013.

[20] B. Morgan, K. Duraisamy, N. Nguyen, S. Kawai, and S. K. Lele. Flow physics and rans modelling of oblique shock/turbulent boundary layer interaction. *Journal of Fluid Mechanics*, 729:231–284, 2013.

[21] J. D. Ott, D. C. Kenzakowski, and S. M. Dash. Evaluation of turbulence modeling extensions for the analysis of hypersonic shock wave boundary layer interactions. *AIAA SciTech Forum , AIAA 2013-0983*, 2013.

[22] E. Parish, D. S. Ching, C. Jordan, G. Nicholson, N. E. Miller, S. Beresh, M. Barone, N. Gupta, and K. Duraisamy. Data-driven turbulent prandtl number modeling for hypersonic shock–boundary-layer interactions. *AIAAJ*, 2024.

[23] S. Pirozzoli and F. Grasso. Direct numerical simulation of impinging shock wave turbulent boundary layer interaction at m=2.25. *Physics of Fluids 18, 065113*, 2006.

[24] S. Priebe and P. M. Martin. Low-frequency unsteadiness in shock wave–turbulent boundary layer interaction. *Journal of Fluid Mechanics*, 699:1–49, May 2012.

[25] H. Rathi and K. Sinha. Simulation of hypersonic shock-boundary layer interaction using shock-strength dependent turbulence model. *AIAAJ*, 62(9), 2024.

[26] C. L. Rumsey. Compressibility considerations for k-w turbulence models in hypersonic boundary-layer applications. *Journal of Spacecraft and Rockets*, 47(1):1–20, 2010.

[27] J. L. Steger and R. F. Warming. Flux vector splitting of the inviscid gasdynamic equations with application to finite-difference methods. *Journal of Computational Physics*, 40:263–293, April 1981.

[28] P. K. Subbareddy and G. V. Candler. A fully discrete, kinetic energy consistent finite volume scheme for compressible flows. *Journal of Computational Physics*, 28:1347–1364, 2009.

[29] E. Touber and N. D. Sandham. Large-eddy simulation of low-frequency unsteadiness in a turbulent shock-induced separation bubble. *Theoretical Computational Fluid Dynamics*, 23:79–107, 2009.

[30] X. I. A. Yang and K. P. Griffin. Grid-point and time-step requirements for direct numerical simulation and large-eddy simulation. *Physics of Fluids*, 33, 2021.

[31] P. Zhang, Z. Wan, N. Liu, D. Sun, and X. Lu. Wall-cooling effects on pressure fluctuations incompressible turbulent boundary layers from subsonic to hypersonic regimes. *Journal of Fluid Mechanics*, 946, 2022.

DISTRIBUTION

Email—Internal

Name	Org.	Sandia Email Address
Cory Stack	1541	cstack@sandia.gov
Ross Wagnild	1511	rmwagni@sandia.gov
Technical Library	1911	sanddocs@sandia.gov

This page intentionally left blank.

Sandia National Laboratories